CHEMISTRY OF MATERIALS

Article

pubs.acs.org/cm

Citrate-Capped $Cu_{11}In_9$ Nanoparticles and Its Use for Thin-Film Manufacturing of CIS Solar Cells

Christian Kind,[†] Claus Feldmann,*[,†] Aina Quintilla,[‡] and Erik Ahlswede*[,‡]

[†]Institut für Anorganische Chemie, Karlsruhe Institute of Technology (KIT), Engesserstrasse 15, D-76131 Karlsruhe, Germany

[‡]Zentrum für Sonnenenergie- und Wasserstoff-Forschung Baden-Württemberg (ZSW), Industriestrasse 6, D-70565 Stuttgart, Germany

ABSTRACT: Intermetallic $Cu_{11}In_9$ nanoparticles with diameters of 10−30 nm were prepared via a facile, easy-to-scale-up polyol-mediated synthesis. Citrate is used as surface-capping and guarantees for efficient stabilization of the $Cu_{11}In_9$ nanoparticles against oxidation in suspension and of powder samples in contact to air. Moreover, the citrate-capping suppresses particle-to-particle agglomeration and allows to prepare high-quality suspensions and even to redisperse $Cu_{11}In_9$ powder samples. The latter is essential to obtain stable inks with precise element composition that can be directly used for thin-film deposition via doctor blading. Based on as-deposited thin-films, high-quality $CuInSe_2$ (CIS) solar cells with power-conversion efficiencies up to 7% were produced by a simple and low-cost, vacuum-free selenization process without the need of additional reducing or sintering processes. $Cu_{11}In_9$ nanoparticles and CIS thin-films as well as the completed solar cells were characterized by various independent analytical tools, including electron microscopy (SEM/STEM), DLS, FT-IR spectroscopy, EDX, XFA, XRD, and SIMS/SNMS.

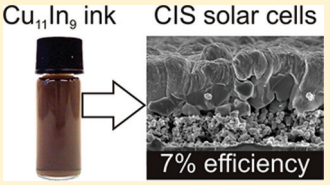

KEYWORDS: *$Cu_{11}In_9$, nanoparticles, thin-film deposition, CIS, solar cell, efficiency*

INTRODUCTION

$CuInSe_2$-based (CIS: copper indium selenide) solar cells represent the most efficient thin-film solar cells with record values close to 15%.[1] For small areas, even 20% has been reported if gallium is also incorporated (so-called CIGS, copper indium gallium selenide).[2] CIS layers are conventionally deposited via high-vacuum techniques utilizing either thermal coevaporation of the elements, including selenium,[3] or via sequential sputtering of Cu and In with subsequent selenization.[4,5]

In recent years, vacuum-free deposition of suitable precursor pastes has attracted increasing attention in view of a low-cost, high-throughput production of CIS thin-film solar cells.[6] One possibility for paste formulation is to use nanoparticles which consist of the relevant metal selenides, metal oxides or elemental metals.[7] This measure takes advantage of the high reactivity of nanoparticles and the possibility to define the composition already on an atomic scale.[8,9] Here, most publications report on nanoparticles that have been directly synthesized via coprecipitation reactions to obtain already mixed ternary Cu−In selenides or quaternary Cu−In−Ga selenides.[9−16]

Although the solid-state diffusion of Cu^{2+} and In^{3+} in metal oxides and metal selenides as CIS precursors is slow, intermixing of phases and healing of pores between the initial nanoparticles is difficult and can significantly reduce solar-cell performance and efficiency. Alternatively, the nanoscaled elemental metals Cu and In can serve as more reactive precursors. While converting such Cu−In thin films via subsequent gas-phase selenization to CIS, the interparticular pores are filled because of the huge volume expansion when reacting metals to metal selenides. Insufficient intermixing of differently composed nanoparticles can however still cause partial deficiencies of the one or other component. Combining both metals to intermetallic Cu−In nanoparticles could elude the above restriction and allow for real homogeneous intermixing of Cu and In on the atomic scale. Subsequent selenization could than yield dense and highly crystalline CIS thin-films without the need of elaborate thermal sintering processes. Such an approach was first investigated by Basol et al.[17] and Norsworthy et al.[18] applying melt-atomization techniques and subsequent ball milling to obtain micrometer-sized Cu−In powders. Promising efficiencies above 10% were demonstrated, but only by using the severely toxic H_2Se for the selenization reaction. Mixtures of nanoscaled In and $Cu_{11}In_9$ with however broad size distribution (10−100 nm) have been recently presented by Chen et al.[19,20] These particles were stabilized by poly(N-vinylpyrrolidone) as a polymer and converted to $CuInS_2$ with limited solar-cell efficiency (≤1.4%). And finally, Liu et al. synthesized CuIn and Cu_2In nanoparticles, 40−60 nm in diameter via chemical coreduction in ethylene glycol.[21] Although detailed studies regarding CIS thin-film preparation and selenization were performed, solar cells were not manufactured here.

In sum, phase homogeneity, density, and crystallinity of thin films, contamination with oxygen due to precursor hydrolysis/oxidation or carbon stemming from thermal decomposition of organic cappings are still open questions. Thus, alternative

Received: August 19, 2011
Revised: October 27, 2011
Published: October 31, 2011

concepts and materials are substantial for significantly increasing the efficiency of CIS solar cells made from nanoparticle precursors. In the following, we report on a facile, low-cost preparation of CIS solar cells, involving high-quality, citrate-capped $Cu_{11}In_9$ nanoparticles, straightforward precursor thin-film deposition, and atmospheric selenization procedure. The resulting CIS thin films show very promising power-conversion efficiencies up to 7%.

EXPERIMENTAL SECTION

Materials, Synthesis, and Thin-Film Deposition. *General.* All chemicals were applied as received. This includes: copper(II)-chloride dihydrate (99%, Riedel de Haën); indium(III)chloride tetrahydrate (99.9%, Aldrich); sodium borohydride (95%, Riedel de Haën); disodium citrate hydrate (99%, Aldrich); diethylene glycol (≥99%, Merck); ethanol (98%, Seulberger). Aqueous solutions were prepared by using demineralised water.

Synthesis of $Cu_{11}In_9$ Nanoparticles. A typical synthesis was performed under dynamic nitrogen purging in order to exclude moisture and oxygen during the reaction; 213.4 mg (1.25 mmol) of $CuCl_2{\cdot}2H_2O$, 366.6 mg (1.25 mmol) of $InCl_3{\cdot}4H_2O$, and 500.0 mg (1.9 mmol) of disodium citrate hydrate were dissolved in 100 mL of diethylene glycol and heated to 100 °C under vigorous stirring. Meanwhile, 284.0 mg (7.50 mmol) of $NaBH_4$ was dissolved in 2.0 mL of demineralized water. When $NaBH_4$ was completely dissolved, this solution was injected to the first-made Cu(II)−In(III)−citrate solution. With this measure, the color of the suspension instantaneously turned greyish black due to the formation of $Cu_{11}In_9$ nanoparticles. The mixture was stirred for 15 min at 100 °C. After natural cooling to room temperature, the as-prepared nanoparticles were collected by centrifugation and washed three times by sequential redispersion in and centrifugation from ethanol. Colloidally stable suspensions were obtained by redispersing the washed nanoparticles in ethanol or isopropanol; powder samples were yielded by drying the solid remnant for 12 h at ambient temperature in air. The $Cu_{11}In_9$ nanoparticles were obtained with a yield of 145 mg (65% based on 1.25 mmol of Cu and 1.25 mmol of In).

Preparation and Processing of $Cu_{11}In_9$ Inks. Suitable suspensions were obtained by redispersing $Cu_{11}In_9$ powders in ethanol with a solid load of typically 200−250 mg mL^{-1} directly before the coating step. Homogeneous precursor films with dry film thicknesses of about 1−2 μm were deposited with freshly prepared $Cu_{11}In_9$ suspensions via doctor blading, using an Erichsen film applicator and an adjustable blade by Zehntner on Molybdenum covered sodalime glass substrates of 1 mm thickness.

Selenization of Thin Films and Solar Cell Preparation. To convert the precursor films to chalcopyrite CIS absorber layers, selenization of the thin films was performed in a tube furnace in nitrogen-diluted selenium vapor, slightly below ambient pressure and similar to the setups described in ref 22. A continuous flux of nitrogen carries the selenium vapor along the sample reaction zone. The intrinsic temperature gradient within the furnace was used to establish a sample temperature of about 550 °C within 60 min, whereas the crucible with the elemental selenium was placed at the edge region of the furnace at about 400−500 °C.

The CIS absorber layers were further treated by selective KCN etching to remove undesired binary CuSe phases, which would typically lead to shunted cell behavior due to its good conductivity. The CIS absorber layers were completed by a wet-chemically processed CdS buffer layer, a sputtered ZnO buffer layer (*i*-ZnO) and a transparent ZnO:Al front-contact layer to obtain functional solar cells using standard procedures as described in ref 23.

Materials Characterization and Analytical Tools. Dynamic light scattering (DLS) was performed with a Nanosizer ZS from Malvern Instruments (equipped with a He−Ne laser (633 nm), detection via noninvasive backscattering at an angle of 173°, 256 detector channels, polystyrene cuvettes). For analysis, the as-prepared $Cu_{11}In_9$ nanoparticles were redispersed in ethanol by ultrasonic treatment for 15 min.

Scanning electron microscopy (SEM) was performed on a Zeiss Supra 40 VP, using an acceleration voltage of 20 kV and a working distance of 2 mm to analyze the size distribution and shape of the $Cu_{11}In_9$ nanoparticles. All samples were prepared by evaporating a single drop of a dispersion of the as-prepared $Cu_{11}In_9$ nanoparticles in ethanol at room temperature in air. The thin-film morphology of precursor layers, selenized layers and completed solar cells were studied with a XL30 SFEG Sirion from FEI Company, using a 5 kV acceleration voltage and working distances of 5.9, 4.3, and 3.4 mm.

Scanning transmission electron microscopy (STEM) was conducted on a Zeiss Supra 40 VP, using an acceleration voltage up to 30 kV and a working distance of 4 mm. STEM samples were prepared on holey carbon-film copper-grids at room temperature. Mean diameters of the nanoparticles were deduced by statistical evaluation of about 100 particles. Note that systematically different diameters obtained by SEM and STEM imaging are related to different electron-detection modes and interaction volumes of the primary electrons with the sample. While SEM images are based on backscattered secondary electrons that were detected by an in-lens detector, only transmitted electrons are collected in the STEM mode of operation.

Energy-dispersive X-ray (EDX) analysis was also conducted on a Zeiss Supra 40 VP electron microscope equipped with a Sapphire Si(Li) detecting unit from EDAX, using an acceleration voltage of 20 kV and a working distance of 8.5 mm. For this purpose about 30 mg of dried $Cu_{11}In_9$ powder was pressed to a thin pellet. Quantitative spectra analysis was performed with the Genesis EDX software.

X-ray fluorescence analysis (XFA) was performed at 10^{-1} mbar on an EAGLE XXL system, equipped with an energy-dispersive Si(Li) detector and a 50 kV Rh X-ray source.

X-ray powder diffraction (XRD) analysis was carried out with a Stoe Stadi-P diffractometer using Ge-monochromatized Cu−$K_{\alpha 1}$ radiation.

Fourier-transform infrared spectra (FT-IR) were recorded on a Bruker Vertex 70 FT-IR spectrometer using KBr pellets. For direct comparison, 400 mg of dried KBr were carefully pestled with 0.3 mg of the sample and pressed to a thin pellet. In addition, spectra of the as-prepared $Cu_{11}In_9$ nanoparticles were subjected to a correction of scattering effects to allow for comparison to reference spectra.

Current−voltage curves were measured using a Keithley 238 source-measuring unit under simulated AM 1.5 global solar irradiation with an ORIEL sun simulator at 100 mW cm^{-2} to extract the basic solar-cell characteristics from devices, approximately 0.24 cm^2 in size.

External quantum efficiency measurements (EQE) were performed using a setup from Optosolar.

Secondary ion mass spectrometry (SIMS) depth profiles of oxygen and carbon composition and secondary neutral mass spectrometry (SNMS) of copper, indium, selenium, and molybdenum were made with a SSM 200 from Leybold.

RESULTS AND DISCUSSION

1. Fundamental Characterization of $Cu_{11}In_9$ Nanoparticles. $Cu_{11}In_9$ nanoparticles were prepared by simultaneous reduction of Cu^{2+} and In^{3+} with $NaBH_4$ in diethylene glycol (DEG) as a solvent. Disodium citrate was involved as a surface-capping and colloidal stabilizer to control the nucleation of the $Cu_{11}In_9$ nanoparticles as well as to suppress the agglomeration of nanoparticles. Right after injection of $NaBH_4$, a greyish black suspension was obtained, indicating the formation of the intermetallic compound. Finally, the as-prepared nanoparticles were collected via centrifugation and washed carefully via sequential redispersion in and centrifugation from ethanol. Colloidally stable suspensions of as-prepared $Cu_{11}In_9$ were obtained by redispersing the washed nanoparticles in ethanol or isopropanol by ultrasound treatment. Adequately diluted suspensions (i.e., $Cu_{11}In_9 \leq 10$ wt.-%) do not show any appreciable sedimentation for weeks (Figure 1). Powder samples were obtained by drying the solid remnant for

dx.doi.org/10.1021/cm2024668 | *Chem. Mater.* 2011, 23, 5269−5274

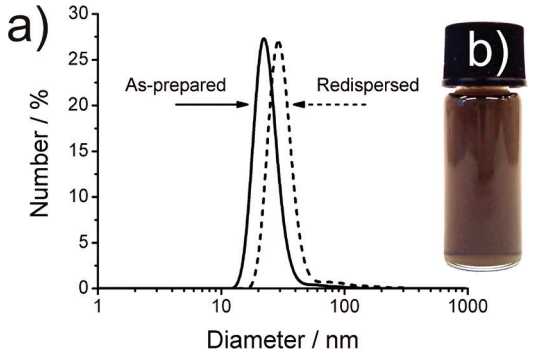

Figure 1. Size and size distribution of as-prepared $Cu_{11}In_9$ nanoparticles and of redispersed dried powder samples (according to DLS) and photo of suspension (in ethanol).

12 h at ambient temperature in air with a yield of about 65% on the laboratory scale.

Size, size distribution, and degree of agglomeration of the as-prepared $Cu_{11}In_9$ were investigated by dynamic light scattering (Figure 1). To this concern, a size distribution of 15−40 nm and a mean hydrodynamic diameter of 23(5) nm were obtained. Electron microscopy (SEM, STEM) confirms size and size distribution of the intermetallic nanoparticles. Thus, SEM overview images show a manifold of uniform nanoparticles with a diameter ranging from 7 to 30 nm and a mean value of 15(5) nm (Figure 2a). Bright-field STEM images

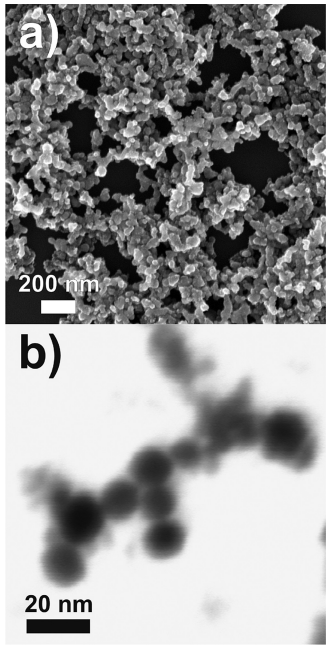

Figure 2. Electron microscopy of as-prepared $Cu_{11}In_9$ nanoparticles: (a) SEM overview image; (b) detailed bright-field STEM image.

finally indicate the presence of separated nanospheres with a mean diameter of 13(4) nm (Figure 2b). When taking the hydrodynamic diameter as obtained by DLS into account, the lower diameter stemming from SEM and STEM is well in accordance to the expectation.

X-ray powder diffraction pattern of the as-prepared nanoparticles exhibit all characteristic Bragg peaks of the intermetallic compound $Cu_{11}In_9$ (Figure 3a).[24] Self-evident impurities such as the elemental metals (i.e., Cu, In) or the corresponding metal oxides (e.g., $Cu(OH)_2$, $In(OH)_3$, Cu_2O, CuO, In_2O_3) are not observed. Because of a certain overlap of the most intense Bragg peaks, a determination of the crystallite size via Scherrer's equation is only possible with limited significance and was therefore not performed. XRD pattern of $Cu_{11}In_9$ powder samples, stored for 12 month in contact to air, appear identical to the as-prepared sample (Figure 3a). The absence of any impurity reflection (i.e., due to crystalline impurities) and any broadening of the peak widths (i.e., due to reaction of crystalline $Cu_{11}In_9$ to noncrystalline impurities) indicate the stability of the citrate-capped $Cu_{11}In_9$ against oxidation. EDX analysis was involved to further confirm the composition of the intermetallic nanoparticles (Figure 3b). With values of 54.8 at % (Cu) and 45.2 at % (In), the composition can be deduced to $Cu_{11.00}In_{9.07}$ which is in good agreement with the expected stochiometry of the $Cu_{11}In_9$ phase.[25] The observation of carbon and oxygen as additional elements is attributed to the presence of citrate as a surface-capping. The low-intensity peak at 1.53 keV, moreover, represents the escape-peak of indium. Altogether, formation of $Cu_{11}In_9$ as a pure phase is surprising since bulk-$Cu_{11}In_9$ has been reported as stable only in the temperature range of 157−310 °C.[26] On the other hand, it is well-accepted that the phase stability of nanomaterials can be different from the bulk phase,[27] so that $Cu_{11}In_9$ is here obtained at a reaction temperature of just 100 °C and as well stable at room temperature.

FT-IR spectra of the as-prepared $Cu_{11}In_9$ nanoparticles clearly evidence the presence of citrate as a surface capping. The characteristic vibrations at 3650−3300 cm^{-1} (ν(OH)), 2950−2850 cm^{-1} (ν(CH)) and 1750−1250 cm^{-1} (ν(COO)) are well in agreement to the spectrum of bulk sodium citrate as a reference (Figure 4). As the $Cu_{11}In_9$ nanoparticles were washed carefully before drying and preparing the IR samples, this finding indicates that citrate is indeed adsorbed on the particle surface. This surface-capping guarantees for an efficient stabilization and passivation of the intermetallic compound. In fact, such citrate-capping is well-known to control nucleation and colloidal stability of nanoparticles.[28−30] The oxidation stability of less-noble metals applying citrate as a surface-capping has been recently shown in the case of elemental indium.[31]

2. Thin-Film Deposition of $Cu_{11}In_9$ Nanoparticles and Selenization Process. An essential advantage of applying citrate-capped $Cu_{11}In_9$ nanoparticles is related to facile ink preparation, thin-film deposition, and chemical conversion to CIS. Thus, the citrate-capping allows for easy redispersion even of dried $Cu_{11}In_9$ powder samples. Note that mean particle size (23(5) and 34(5) nm) and particle size distribution remain very similar and below 100 nm for as-prepared $Cu_{11}In_9$ nanoparticles and redispersed $Cu_{11}In_9$ dry powders (Figure 1). The prepared inks are stable for hours guaranteeing for an adequate time period for processing. This finding underlines the role of the citrate-capping because metal nanoparticles especially are known to agglomerate irreversibly during drying if the surface is not adequately stabilized.[32]

Facile redispersion of $Cu_{11}In_9$ powders furthermore allows to precisely adjust the nanoparticle concentration in terms of ink formation. Based on colloidally stable suspensions containing nonagglomerated nanoparticles, $Cu_{11}In_9$ thin-films can be easily deposited via the doctor blading technique. As a result, homogeneous layers with matte-grayish appearance were obtained. The layer thickness can be increased to the requested

dx.doi.org/10.1021/cm2024668 | Chem. Mater. 2011, 23, 5269−5274

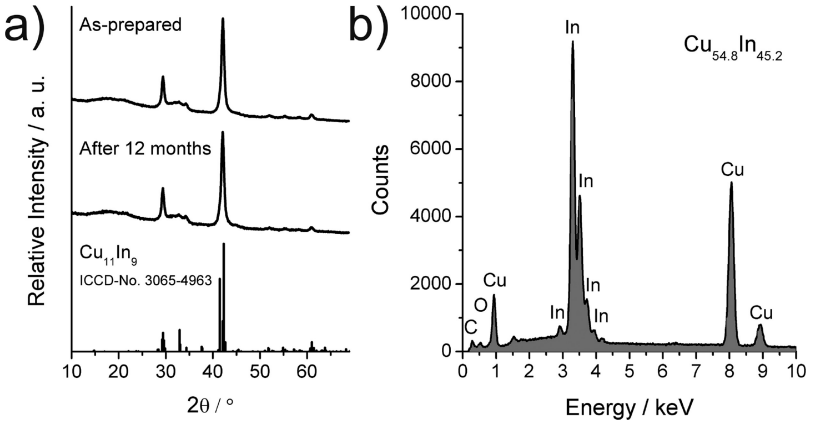

Figure 3. Composition and oxidation stability of intermetallic $Cu_{11}In_9$ nanoparticles: (a) XRD powder diffraction pattern of as-prepared $Cu_{11}In_9$ as well as the same sample after storing for 12 month in contact to air (bulk-$Cu_{11}In_9$, ICCD-No. 3065−4963, as a reference); (b) EDX analysis of as-prepared $Cu_{11}In_9$.

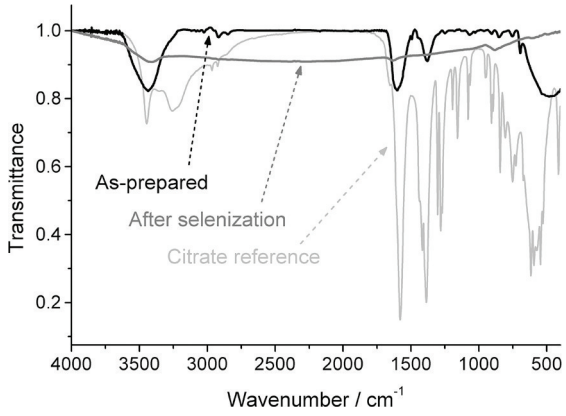

Figure 4. Citrate capping on $Cu_{11}In_9$ according to FT-IR spectra: as-deposited $Cu_{11}In_9$ thin-film (black line); $Cu_{11}In_9$ thin-film after selenization (dark gray line) and bulk sodium citrate (light gray line) as a reference.

value via on-top deposition of additional blade runs. Figure 5a shows cross-sectional SEM images of such as-deposited $Cu_{11}In_9$ thin films with a thickness of 2−3 μm. Although agglomerated in the dried and porous thin film, size and shape of the initial $Cu_{11}In_9$ nanoparticles are still clearly visible.

The as-deposited $Cu_{11}In_9$ thin-films do not need any additional post-treatment (e.g., sintering, densification or reducing procedures), except for the selenization process. Here, the stability of the citrate-capped $Cu_{11}In_9$ nanoparticles toward oxidation is highly relevant. In contrast to alternative precursor materials and strategies of layer deposition,[33] an additional reduction in H_2 atmosphere does not improve the final solar-cell performance. And finally, neither any phase segregation nor any change in composition is observed across the as-deposited $Cu_{11}In_9$ precursor thin-films (Table 1). Thus, X-ray fluorescence analysis (XFA) based on more than 50 points of measuring on the as-deposited layer with a Cu:In ratio of 51(3):49(3) evidence a very uniform composition with a slight excess of copper. This is a clear advantage in comparison to alternative approaches based on mixed inks, containing for instance the metals Cu and In as separate nanoparticles.[18−20] For the latter case, demixing and phase segregation during the blading process is often observed and leads to an inhomogeneous element distribution.

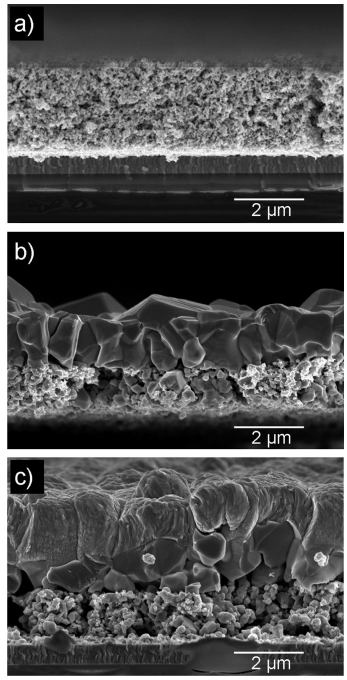

Figure 5. Assembly of a CIS solar cell shown with SEM cross sections: (a) $Cu_{11}In_9$ precursor layer on sputtered Molybdenum double layer; (b) $Cu_{11}In_9$ thin-film after selenization; (c) completed CIS solar cell with buffer layers (*i*-ZnO and CdS) and front contact (ZnO:Al) on top.

Table 1. X-ray Fluorescence Analysis of As-Deposited $Cu_{11}In_9$ Precursor Layers and of Selenized CIS Layer after Cell Preparation[a]

	Cu (at %)	In (at %)	Se (at %)	Cu:In	no. of measuring points
$Cu_{11}In_9$ precursor layer	51 ± 1	49 ± 1		1.05 ± 0.04	54
CIS solar cell	22 ± 1	26 ± 1	52 ± 1	0.81 ± 0.03	3

[a]Analysis of solar cells was performed after KCN etching process to remove undesired CuSe or Cu_2Se phases, leading to a slightly Cu poor composition.

dx.doi.org/10.1021/cm2024668 | *Chem. Mater.* 2011, 23, 5269−5274

3. Characterization and Performance of CIS Solar Cells. The selenization of the $Cu_{11}In_9$ precursor films takes place in a standard tube-furnace setup under selenium atmosphere. According to XRD measurements of the selenized films, the $Cu_{11}In_9$ nanoparticles were completely converted into the semiconducting ternary polycrystalline chalcopyrite $CuInSe_2$ (Figure 6a). Bragg peaks that eventually may indicate

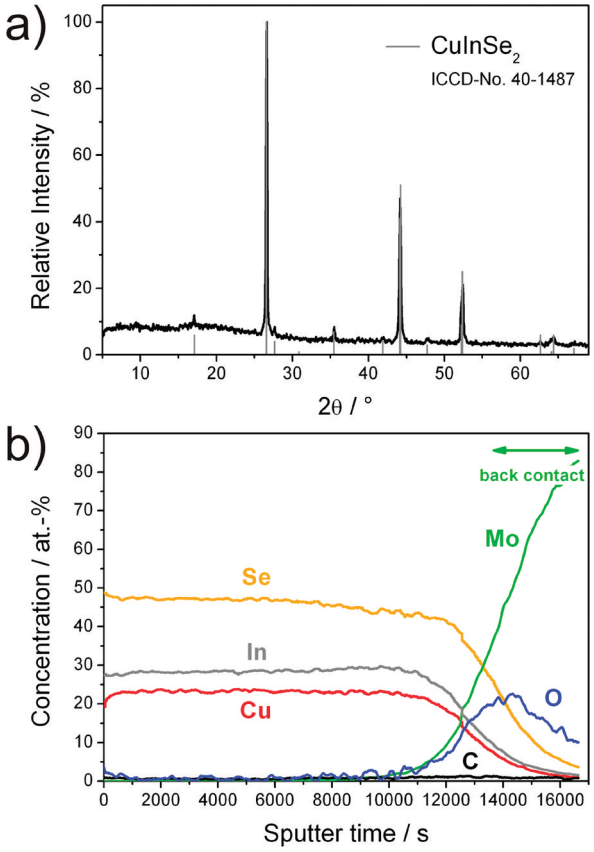

Figure 6. Chemical composition of the completed CIS solar cell: (a) XRD pattern of the $CuInSe_2$ absorber material (bulk-$CuInSe_2$, ICCD-No. 40−1487, as a reference); (b) relative atomic-composition depth profile (according to SIMS/SNMS). Analysis was performed after etching of buffer layers (*i*-ZnO and CdS) and front contact (ZnO:Al) with HCl (2%).

self-evident impurity phases such as Cu, In, $Cu_{11}In_9$, other intermetallic phases or oxides are not observed. However, an often observed finding is the formation of a dense, crystalline top layer with a bottom layer consisting of much smaller grains underneath.[18−20] Here, 1.4−1.6 μm-sized CIS grains were found as a top layer as well. Particles with 100−500 nm in diameter, on the other hand, form a 1.2−1.4 μm thick bottom-layer (Figure 5b). As discussed recently,[33] there is in principle enough Se available to penetrate through the porous precursor layer. This is indicated by the fact that in some cases, even the Mo back contact is selenized under formation of $MoSe_2$. Obviously, only the grain growth of the CIS bottom layer is inhibited. This view is validated by SNMS depth-profile analysis (Figure 6b), showing a uniform composition without any apparent difference between the two layers. Only a slight increase of the indium concentration in the bottom layer indicates the border to the smaller-sized CIS grains.

Surprisingly low carbon and oxygen contents of the CIS layer point to the fact that the citrate-capping of the $Cu_{11}In_9$ precursor was indeed completely removed during selenization. This points to an additional advantage of the citrate-capping, namely the complete thermal decomposition into volatile compounds (e.g., methyl maleic anhydride, acetone) even under oxygen-free conditions.[34,35] FT-IR spectra confirm the absence of citrate in the selenized layer (Figure 4). In contrast to the initial $Cu_{11}In_9$ nanoparticles and the as-deposited thin-films, the characteristic vibrations related to citrate (ν(CH): 2950−2850 cm^{-1}, ν(COO): 1750−1250 cm^{-1}, fingerprint area: 1250−500 cm^{-1}) are vanished now. Besides the colloidal stability of the $Cu_{11}In_9$ nanoparticles in suspension, the citrate-capping is therefore also highly beneficial in view of a well-directed removal, allowing for straightforward sintering of homogeneously composed and contamination-free CIS thin-films. The influence of the selenization parameters (e.g., temperature, duration, Se pressure, Se concentration) on film conversion and cell performance are, however, rather complex and the subject of ongoing in-depth work.

The CIS solar cells were finally completed by topping with buffer layers (*i*-ZnO and CdS) and a front contact (ZnO:Al) (Figure 5c). Thereafter, current−voltage (I−V) curves and external quantum efficiency (EQE) were characterized (Figure

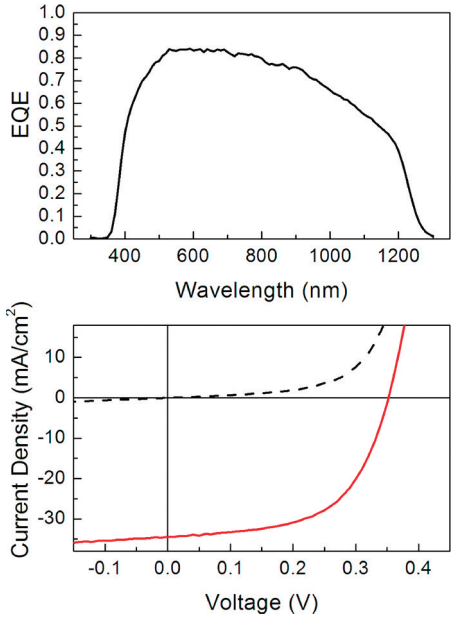

Figure 7. External quantum efficiency (top) and current−voltage characteristics (bottom) of the CIS record cell: efficiency, 7.0%; open circuit voltage, 352 mV; fill factor, 57%; current density, 34.3 mA cm^{-2}.

7). Again, the chemical composition of selenized and KCN-etched CIS films (i.e., to remove undesired binary CuSe phases) was determined and resulted in 22 ± 1 at % Cu, 26 ± 1 at % In and 52 ± 1 at % Se (Table 1), representing a slightly Cu deficient stochiometry as is desired for high-quality, p-type CIS absorber films. The resulting CIS solar cells exhibit reproducible efficiencies well above 4% for corrected aperture area, with a record value of 7%. As can be seen from the I−V curves, the current density (J_{sc}) with 34.3 mA cm^{-2} is relatively high as confirmed by external quantum efficiency (EQE) measurements (Figure 7). The band gap with 0.9 eV is lower as compared to about 1.0 eV as reported for bulk-$CuInSe_2$.[1] As the band gap directly influences the open circuit voltage (V_{oc}), this

dx.doi.org/10.1021/cm2024668 | *Chem. Mater.* 2011, 23, 5269−5274

finding can to some extend explain both, the relatively high current density and the rather poor V_{oc} of 350 mV. The latter certainly is also influenced by recombination losses at the interfaces. Especially the poor morphology of the bottom layer could lead to an enhanced series resistance and recombination losses. Further improvements, especially of the V_{oc} value, but also of the fill factor (FF), bear the potential to even further increase the solar-cell performance and efficiency. Currently, we honestly have to conclude that it remains unclear if the frequently observed CIS bottom layer containing nonoptimal grain sizes is completely inactive, leaving the photovoltaic process only to the top-layer. Taking this situation into account, the already obtained external quantum efficiencies are even more encouraging.

CONCLUSIONS

Intermetallic $Cu_{11}In_9$ nanoparticles, 10−30 nm in diameter were synthesized via a polyol-mediated synthesis. Citrate-capping of the as-prepared nanoparticles prevents agglomeration and air oxidation, and furthermore allows for complete redispersion even of dried $Cu_{11}In_9$ powders. As a result, the nanoparticle concentration can be precisely adjusted when redispersing as an ink for subsequent doctor blading and layer deposition.

Based on the as-deposited intermetallic $Cu_{11}In_9$ nanoparticles, $CuInSe_2$ (CIS) films with thicknesses of 2−3 μm were realized via low-cost vacuum-free selenization. The resulting two-layer structure was studied by electron microscopy as well as by SIMS/SNMS and did not show any significant difference in composition between bottom- and top-layer. Accordingly, the $Cu_{11}In_9$ precursor was completely transformed into the polycrystalline chalcopyrite $CuInSe_2$. No carbon and very low oxygen content were detected after the selenization process, indicating an easy removal of the citrate-capping as well as the oxidation stability of the initial $Cu_{11}In_9$ nanoparticles. Additional sintering or reduction processes are not necessary and facilitate the complete process of solar-cell processing. The completed CIS solar cells manufactured via the $Cu_{11}In_9$ precursor with up to 7% exhibit very promising power-conversion efficiencies. Further optimization of the solar-cell system, especially addressing CIS grain growth and CIS back-contact interface, suggest an even higher efficiency and overall performance.

AUTHOR INFORMATION

Corresponding Author

*E-mail: claus.feldmann@kit.edu (C.F.); erik.ahlswede@zsw-bw.de (E.A.). Tel: (+)49-721-60842855 (C.F.); (+)49-711-7870247 (E.A.). Fax: (+)49-721-60844892 (C.F.); (+)49-711-7870230 (E.A.).

ACKNOWLEDGMENTS

The authors are grateful to the German Ministerium für Bildung und Forschung (BMBF) for funding within the project "*Nanopartikuläre Dünnschicht-Solarzellen − Grundlagen und Prozesstechnologie (NanoPV)*". C.K. and C.F. further acknowledge the Center of Functional Nanostructures (CFN) of the Deutsche Forschungsgemeinschaft (DFG) at the Karlsruhe Institute of Technology (KIT) for financial support.

REFERENCES

(1) AbuShama, J. A. M.; Johnston, S.; Moriarty, T.; Teeter, G.; Ramanathan, K.; Noufi, R. *Prog. Photovolt. Res. Appl.* **2004**, *12*, 39.
(2) Repins, I.; Contreras, M. A.; Egaas, B.; DeHart, C.; Scharf, J.; Perkins, C. L.; To, B.; Noufi, R. *Prog. Photovolt. Res. Appl.* **2008**, *16*, 235.
(3) Gabor, A. M.; Tuttle, J. R.; Albin, D. S.; Contreras, M. A.; Noufi, R.; Hermann, A. M. *Appl. Phys. Lett.* **1994**, *65*, 198.
(4) Marudachalam, M.; Hichri, H.; Klenk, R.; Birkmire, R. W.; Shafarman, W. N.; Schultz, J. M. *Appl. Phys. Lett.* **1995**, *67*, 3978.
(5) Probst, V.; Stetter, W.; Riedl, W.; Vogt, H.; Wendl, M.; Calwer, H.; Zweigart, S.; Ufert, K.-D.; Freienstein, B.; Cerva, H.; Karg, F. H. *Thin Solid Films* **2001**, *387*, 262.
(6) Hibberd, C. J.; Chassaing, E.; Liu, W.; Mitzi, D. B.; Lincot, D.; Tiwari, A. N. *Prog. Photovolt. Res. Appl.* **2010**, *18*, 434.
(7) Goesmann, H.; Feldmann, C. *Angew. Chem.* **2010**, *122*, 1402; *Angew. Chem., Int. Ed.* **2010**, *49*, 1362.
(8) Eberspacher, C.; Fredric, C.; Pauls, K.; Serra, J. *Thin Solid Films* **2001**, *387*, 18.
(9) Kapur, V. K.; Bansal, A.; Le, P.; Asensio, O. I. *Thin Solid Films* **2003**, *431−432*, 53.
(10) Wang, W.; Jin, Z.; Liu, H.; Du, H. *Mater. Lett.* **2011**, *65*, 2895.
(11) Zhang, Y.; Ito, M.; Tamura, T.; Yamada, A.; Konagai, M. *Jpn. J. Appl. Phys.* **2011**, *50*, 04DP12/1.
(12) Lee, J. H.; Chang, J.; Cha, J.-H.; Lee, Y.; Han, J. E.; Jung, D.-Y.; Choi, E. C.; Hong, B. *Eur. J. Inorg. Chem.* **2011**, *5*, 647.
(13) Guo, Q.; Kim, S. J.; Kar, M.; Shafarman, W. N.; Birkmire, R. W.; Stach, E. A.; Agrawal, R.; Hillhouse, H. W. *Nano Lett.* **2008**, *8*, 2982.
(14) Panthani, M. G.; Akhavan, V.; Goodfellow, B.; Schmidtke, J. P.; Dunn, L.; Dodabalapur, A.; Barbara, P. F.; Korgel, B. A. *J. Am. Chem. Soc.* **2008**, *130*, 16770.
(15) Ahn, S.; Kim, K.; Yoon, K. *Curr. Appl. Phys.* **2008**, *8*, 766.
(16) Yoon, S.; Yoon, T.; Lee, K.-S.; Yoon, S.; Ha, J. M.; Choe, S. *Sol. Energy Mater. Sol. Cells* **2009**, *93*, 783.
(17) Basol, B. M. *Thin Solid Films* **2000**, *361−362*, 514.
(18) Norsworthy, G.; Leidholm, C. R.; Halani, A.; Kapur, V. K.; Roe, R.; Basol, B. M.; Matson, R. *Sol. Energy Mater. Sol. Cells* **2000**, *60*, 127.
(19) Chen, G.; Wang, L.; Sheng, X.; Liu, H.; Pi, X.; Yang, D. *J. Alloys Compd.* **2010**, *507*, 317.
(20) Chen, G.; Wang, L.; Sheng, X; Yang, D. *J. Mater. Sci. Mater. Electron.* **2011**, *22*, 1124−1129.
(21) Liu, S.-H.; Chen, F.-S.; Lu, C.-H. *Chem. Lett.* **2010**, *39*, 1333.
(22) Kaelin, M.; Rudmann, D.; Kurdesau, F.; Zogg, H.; Meyer, T.; Tiwari., A. N. *Thin Solid Films* **2005**, *480−481*, 486.
(23) Powalla, M.; Dimmler, B. *Thin Solid Films* **2001**, *387*, 251.
(24) Rajasekharan, T. P.; Schubert, K. *Z. Metallkd.* **1981**, *72*, 275.
(25) Liu, H. S.; Cui, Y.; Ishida, K.; Liu, X. J.; Wang, C. P.; Ohnuma, I.; Kainuma, R.; Jin, Z. P. *J. Phase Equilib.* **2002**, *23*, 409.
(26) Okamoto, H. *J. Phase Equilib.* **2005**, *26*, 645.
(27) Banhart, F.; Ajayan, P. M. *Nature* **1996**, *382*, 433.
(28) Turkevich, J.; Stevenson, P. C.; Hillier, J. *Discuss. Faraday Soc.* **1951**, *11*, 55.
(29) Kobayashi, Y.; Horie, M.; Konno, M.; Rodríguez-González, B.; Liz-Marzán, L. M. *J. Phys. Chem. B* **2003**, *107*, 7420.
(30) Mladenov, M.; Zlatilova, P.; Dragieva, I.; Klabunde, K. *J. Power Source* **2006**, *23*, 803.
(31) Kind, C.; Feldmann, C. *Chem. Mater.* **2011**, DOI: 10.1021/cm202256t.
(32) Grouchko, M.; Popov, I.; Uvarov, V.; Magdassi, S.; Kamyshny, A. *Langmuir* **2009**, *25*, 2501.
(33) Ungelenk, J.; Haug, V.; Quintilla, A; Ahlswede, E. *Phys. Status Solidi RRL* **2010**, *4*, 58.
(34) Barbooti, M. M.; Al-Sammerrai, D. A. *Thermochim. Acta* **1986**, *98*, 119.
(35) Gajbhiye, N. S.; Bhattacharya, U.; Darshane, V. S. *Thermochim. Acta* **1995**, *264*, 219.